Robotic Actuation and Control of A Catheter for Structural Intervention Cardiology

Xiu Zhang, Maria Chiara Palumbo, Francesca Perico, Mattia Magro, Andrea Fortuna, Tommaso Magni, Emiliano Votta, Alice Segato* and Elena De Momi*

***Abstract*— Structural intervention cardiology (SIC) interventions are crucial procedures for correcting heart valves, wall, and muscle form defects. However, the possibility of embolization or perforation, as well as the lack of transparent vision and autonomous surgical equipment, make it difficult for the clinician. In this paper, we propose a robot-assisted tendon-driven catheter and machine learning-based path planner to overcome these challenges. Firstly, an analytical inverse kinematic model is constructed to convert the tip location in the Cartesian space to the tendons' displacement. Then inverse reinforcement learning algorithm is employed to calculate the optimal path to avoid possible collisions between the catheter tip and the atrial wall. Moreover, a closed-loop feedback controller is adopted to improve positioning accuracy in a direct distal position measurement manner. Simulation and experiments are designed and conducted to demonstrate the feasibility and performance of the proposed system.**

I. INTRODUCTION

SIC procedures allows to treat intracardiac pathologies through the transcatheter implantation of repair or replacement devices (Fig. 1). Initially conceived to extend treatment to patients uneligible to open-chest surgery, SIC procedures were becoming increasingly popular as first-line treatment as they are associated with reduced trauma, shorter hospitalization time, and comparable effectiveness vs. open chest surgery structural heart disease (SHDs) [1]. On the other hand, SIC procedures are not ergonomic, technically demanding, as the operator must maneuver the proximal end of the catheter to define the motion of the distal end in the unconstrained and dynamic intracardiac environment, and characterized by a steep learning curve, with the operator experience associated with the procedural success [2]. As a result, complex SIC procedures are accessible only at few excellence clinical centers with highly skilled and experienced operators [3].

The ARTERY project intends to advance the area of SIC by introducing a a variable shared autonomy robotic platform for intra-procedural support, which is currently underdevelopment using the robotization of the commercial MitraClip^{TM} (MC) system as initial benchmark. The MC system allows to treat mitral regurgitation by percutaneously implanting a clip that grasps the valve leaflets (Fig. 1). The clip is deployed by a catheter, which is inserted in the femoral vein, driven to the inferior vena cava, the right atrium and then into the left atrium, where it is steered to target the region of the mitral leaflets to be grasped. One of the project's key goals is to provide reliable autonomous navigation in the left atrium, which can be considered an unconstrained environment due to its shape and size, using *ad hoc* control software and artificial intelligence.

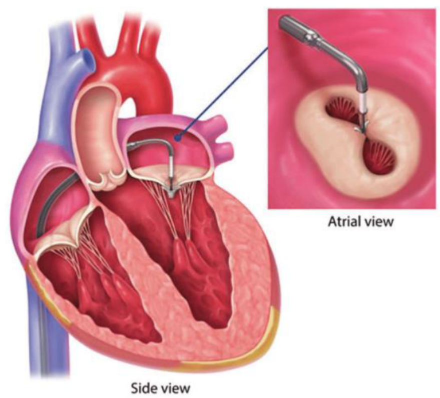

Fig. 1. Positioning of the MC on the mitral valve. The side view shows a four-chamber section of the heart: the catheter arrives from the inferior vena cava (in blue), enters the right atrium, and reaches the left atrium via a trans-septal approach. The positioning of the MC is shown in detail in the atrial view: the clip anchors the free margin of the two mitral leaflets and keeps them locally in contact.

In this paper, we suggested a robotic-assisted approach (Fig. 2) to address the challenge in this research. Firstly, Cosserat rob theory (CRT) was employed for the kinematic model of the tendon-driven robotic catheter, which mapped the tip location in the task space with the tendons' displacement in the actuation space. Then, comparing the recent advances in learning based methods in path planning, we deployed Learning from Demonstration (LfD) algorithm along with Proximal Policy Optimization (PPO) policy for training an artificial intelligent agent to plan an optimized trajectory toward the target position. Furthermore, we designed an autonomous robot-assisted platform based on the commercially-available MC system developed by Abbott, which we combined with our algorithm. Finally, to validate the suggested strategy, extensive experiments were carried out in a patient-specific physical phantom.

This work was supported by the European Union's Horizon 2020 research and innovation program, under the project ARTERY, grant agreement No. 101017140

The authors are with the Department of Electronics, Information and Bioengineering, Politecnico di Milano, Milan 20133, Italy (xiu.zhang, mariachiara.palumbo, francesca.perico, emiliano.votta, alice.segato, elena demomi)@polimi.it

Alice Segato and Elena De Momi are the co-last authors

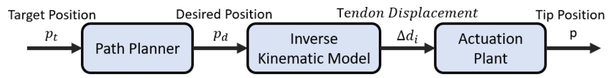

Fig. 2. Workflow of the robotic-assisted system

II. Related works

A. Kinematic Modelling

The coupling between the tendons and the backbone, as well as the kinematic or static assumptions of the backbone, were the key topics of discussion while designing a tendon-driven continuum robot (TDCR). There were two dominant types of structures of attaching tendons on the backbone, which were using two spacer disks to partially constrain the tendon path within each subsegment and using a large inner lumen to guide the tendons along the backbone. Partially constrained tendons were modeled as forces and moments operating on the attached disk. On the other hand, due to the fully constrained tendon path the forces could be equivalent to a distributed load, which is equal and opposite to the internal force of the backbone[4].

The most common approach to model the backbone was the piecewise constant-curvature approximation, in which the section could be assumed to undergo planar deformation. The shape of the robot had been simplified as an arc geometry without the torsion effect [5]. To overcome this problem, Su et al. proposed an approach to approximate a TDCR as a serial robot link by torsion springs. However, the stiffness of the springs and the length of each link were dependent on the external force and moment[6]. Nowadays, the most accurate model was the variable curvature approach, which was a finite element method based on the CRT. The backbone was represented by a fixed number of points with six degrees of freedom, named nodes. The configuration of the TDCR could be estimated by solving the equilibrium equations for all the nodes with the boundary conditions [7], [8].

B. Path Planning

Intracardiac path planning was not well explored in recent studies. In one study, a simple algorithm had been proposed that plans a straight line from the catheter tip to the intracardiac target position. However, the system should be improved by accommodating different curves to avoid anatomical obstacles [9]. Another recent and novel method exploited wall-following algorithm [10]. This approach employed thigmotactic algorithms that achieved autonomous navigation inside the heart by creating low-force contact with the tissue and then following tissue walls to reach a goal location. Its performance on autonomously controlled robotic catheter outperforms that of an experienced clinician. Recently, learning based methods had gained massive attention, and they were also proposed for surgical procedure such as intravascular [11] or neurosurgical [12] cases. Among the learning algorithms, different sub-classes could be distinguished, LfD and Deep Reinforcement Learning (Deep RL) being the two dominant categories. In the LfD paradigm, human demonstrations were used to obtain a reference trajectory for the desired task. In this case, the catheterization demonstrations would be done by an expert surgeon. Subsequently, a learning algorithm is exploited to extract the key features of this trajectory. This enabled the robot to perform the task on its own, even under different conditions [13]. It had been shown that with this kind of algorithm improvements over manual catheterization can be obtained [14]. In autonomous and semi-autonomous intracardiac surgeries, Deep RL could be exploited to overcome the unpredictability of movements and errors introduced by the operator that could affect the accuracy of the traced path.

C. Motion Control

Loschak et al. [15] designed an automatic ultrasound catheter with an EM tracker, four brushed DC motors for each degree of freedom, and a position controller with a 1.6mm position error in the open 3D space. Moreover, Junghwan et al. proposed a Model-free position control algorithm using electromagnetic (EM) tracker and tension feedback. Their cardiac ablation catheter had a minimum position error up to 0.5 ± 0.2mm within 7 ± 2sec [16]. A probabilistic kinematic model of a catheter robot was studied by Bing Yu et al. [17] to take into account intrinsic non-linearities and external disturbance. A proportional–integral–derivative (PID) controller was implemented for closed-loop position control, and the results indicated that a simulated catheter could follow the centerline of the aorta with an accuracy of $1.2 \pm 1.067mm$.

III. Methodology

A. Kinematic model of the catheter

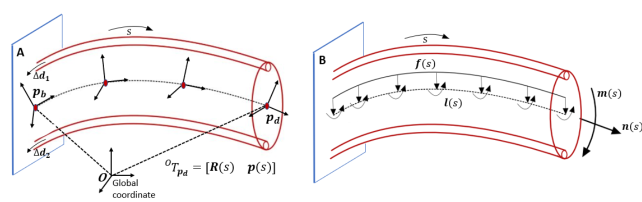

Fig. 3. Sketches of the catheter: (A) Kinematics of the CRT maps the distal position $\mathbf{p_d}$ and tendon displacement $\mathbf{\Delta d_i}$; (B) Free-body diagram of the catheter subjected to external distributed forces $f(s)$ and moments $l(s)$; internal forces $n(s)$ and moment $m(s)$ over the backbone length s are represented.

Kinematics based on CRT is implemented, in which the robotic catheter was assumed to be functioning in a quasi-static process to relate the distal end position ($\mathbf{p_d}$) and tendon displacement ($\mathbf{\Delta d_i}$). The tendons are assumed to follow a continuous curve parallel to the backbone, implying that tendon pathways are totally constrained. A number of nodes positioned along the backbone represent the catheter's configuration, and the deformation of the backbone can be computed using the CRT. The reference frames composed by a rotation matrix ($\mathbf{R}$) and a pose vector ($\mathbf{p}$) are attached to the nodes (Fig. 3 A), and its evolution along the body length (s) was described by means of a system of differential equations:

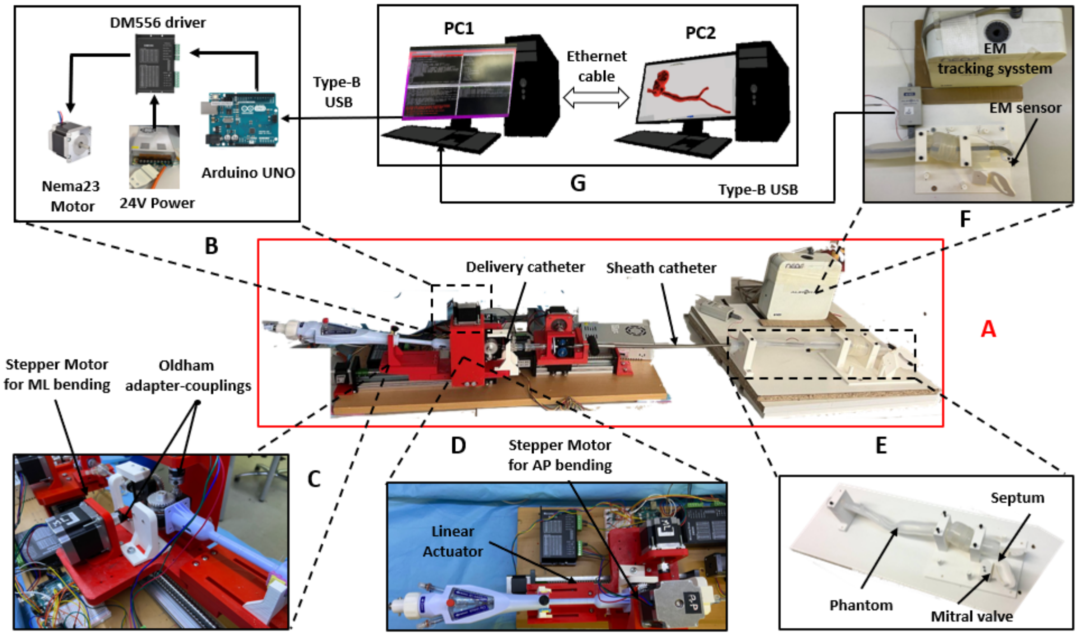

Fig. 4. Complete robotic-assisted surgical system: (A) catheter actuation plant; (B) electrical devices and power source; (C) details of the motorized stabilizer for the bending in the medio-lateral plane; (D) details of the motorized stabilizer for the bending in the antero-posterior plane and the linear actuator; (E) patient-specific physical phantom; (F) EM tracking system and the EM sensor; (G) computers used for running the ROS environment on Ubuntu 20.04 and the Unity simulation on Windows 10.

$$\begin{aligned}\dot{\mathbf{R}}(s) &= \dot{\mathbf{R}}(s)\hat{\mathbf{u}}(s)\\ \dot{\mathbf{p}}(s) &= \mathbf{R}(s)\mathbf{v}(s)\end{aligned} \tag{1}$$

We solve the equilibrium equations between internal forces and moments, $\boldsymbol{n}$(s) and $\boldsymbol{m}$(s), and external forces and moments, $\boldsymbol{f}$(s) and $\boldsymbol{l}$(s), for each node to obtain $\boldsymbol{u}$(s) and $\boldsymbol{v}$(s), which are the values of angular and linear rate of change of each node.

$$\begin{aligned}\dot{\mathbf{n}}(s)+\mathbf{f}(s) &= 0\\ \dot{\mathbf{m}}(s)+\dot{\mathbf{p}}(s)\times\mathbf{n}(s)+\mathbf{l}(s) &= 0\end{aligned} \tag{2}$$

At last, the internal force and moment are related with $\boldsymbol{u}$(s) and $\boldsymbol{v}$(s), exploiting constitutive material laws:

$$\begin{aligned}\mathbf{n}(s) &= \mathbf{R}(s)\mathbf{K}_{se}(s)(\mathbf{v}(s)-\mathbf{v}^{*}(s))\\ \mathbf{m}(s) &= \mathbf{R}(s)\mathbf{K}_{bt}(s)(\mathbf{u}(s)-\mathbf{u}^{*}(s))\end{aligned} \tag{3}$$

where

$$\begin{aligned}\mathbf{K}_{se}(s) &= diag(GA(s),GA(s),EA(s))\\ \mathbf{K}_{bt}(s) &= diag(EI_{xx}(s),EI_{yy}(s),GJ)\end{aligned} \tag{4}$$

$\mathbf{K_{se}(s)}$, $\mathbf{K_{bt}(s)} \in \mathbb{R}^{\mathbf{3\times 3}}$ matrices are stiffness matrices, which are determined by the mechanical properties and the geometry of the catheter. $A(s)$ is the cross sectional area; $I(s)$ and J are the corresponding second moment of area and the polar moment of inertia, respectively. G and E represent the shear modulus and the Young modulus of the material, respectively.

Under the assumption of fully constrained tendon path, these tendons are considered as equivalent distributed force and moment along the entire length of the backbone and integrated as a part of internal force $\boldsymbol{n}$(s) and moment $\boldsymbol{m}$(s) of the backbone. Moreover, the gravity force is treated as a combination of distributed external forces $\boldsymbol{f}$(s) and moments $\boldsymbol{l}$(s) (Fig. 3 B).

Combining equations (1), (2), (3), we obtain the complete set of CRT differential equations, which are numerically solved via Shooting method [18]: the solution is searched for iteratively until boundary conditions are satisfied.

B. Design of the path planner

Path planning is a mathematical problem to find the optimum sequence of valid configurations to move from one point (source) to another point (destination). Path planning algorithms generate a geometric path from the source to the destination, possibly passing through predefined via-points while considering blocked areas [19]. The configuration space is found as a subset of free space. The main challenges of our project in robotic path planning are as follows:

- Convergence, ensuring at least one valid solution by reaching the destination defined as target configuration ($\mathbf{q}_t$).
- Optimality, considering the timing (*time*) and the minimum (*minDist*) and the average (*avgDist*) distance.
- Geometric and movement restrictions of the catheter, evaluating the curvature (*curv*) and the length (*len*).
- Geometric and movement restrictions associated with the intracardiac environment and with obstacles to be avoided (*obst*)

The 3D geometry of the anatomical structures of interest (i.e., right and left atria and ventricles, inferior and superior vena cava, femural veins, pulmonary artery) was reconstructed from a Computed Tomography (CT) scan (dimension $512 \times 512 \times 347$) provided by IRCCS Ospedale San Raffaele, yielding the simulation environment to train a Generative Adversarial Imitation Learning (GAIL) model in pre-operative path planning. Using 3D Slicer software [20], CT images were manually segmented, and 3D reconstructions were subsequently smoothed and filtered with a Gaussian filter. The resulting discretized solid geometries were hollowed in MeshMixer software [21] to obtain the final meshes to create the simulated scene. The anatomical environment in which the agent (i.e., the catheter) moves was finally reconstructed in the Unity 3D game engine [22] .

We used a combination of Behavioral Cloning (BC) [23] and GAIL [24] reward signal to find the optimized pre-operative path from the entry to the target poses. The former method lets the agent reproduce a close copy of the demonstration, whereas the latter deploys an adversarial approach using a discriminative next to a generative network.

The path planner takes in input the starting configuration ($\mathbf{q}_s$) of the agent, consisting in its pose (3 positions and 3 rotations in the 3 axes expressed in Euler angles) and the target configuration ($\mathbf{q}_t$). The output of the path planning algorithm is a pre-operative path ($\mathbf{P}$), i.e., an admissible sequence of agent configurations ($\mathbf{q}_{agent_t}$) from the starting one $\mathbf{q}_{agent_0} == \mathbf{q}_s$ to the target one $\mathbf{q}_{agent_{n-1}} == \mathbf{q}_t$, where n is the number of configurations that generate the path $\mathbf{P}$ and is equal to $\#\mathbf{P}$. Hence, $\mathbf{P}$ can be expressed as:

$$\mathbf{P} = \{\mathbf{q}_{agent_0}, \mathbf{q}_{agent_1}, \ldots, \mathbf{q}_{agent_{n-1}}\} \tag{5}$$

Our catheter represents the agent, that is the learner and the decision maker. It is placed in the environment and it can take actions ($\mathbf{a_t}$), moving towards the target ($\mathbf{a_t}$) with a combination of the translation along its X-direction and the rotation about its Z-direction and Y-direction. With these actions the environment can give positive or negative rewards (r_t), which are usually scalars, to the agent.

The reward function, $R(\tau) = r_t$, associated with each time step, t, is shaped in order to make the agent learn to optimize the path, according to three main requirements:

- agent steps number (t) minimization
- obstacle avoidance with $\mathbf{q}_{agent} \notin obst$
- target position error (tpe) minimization, where tpe is the Euclidean distance between the needle's final position ($\mathbf{p}(\mathbf{q}_{agent})$ and the target position ($\mathbf{p}(\mathbf{q}_t)$),

The reward (r_t) is defined as:

$$r_t = \begin{cases} r_{step_{max}} \text{ if } t \geq t_{max} \\ r_{obst} + r_{step} \text{ if } \mathbf{q}_{agent_t} \in obst \\ r_{target} + r_{TPE} + r_{step} \text{ if } \mathbf{q}_{agent_t} == \mathbf{q}_t \\ r_{step} \text{ otherwise} \end{cases} \tag{6}$$

- A negative reward, $r_{step_{max}}$, is given if the the cumulative number of steps (t) exceeds the predefined maximum number of steps allowed for (t_{max}).
- A negative reward, $r_{step} = -\frac{1}{t_{max}}$, is given at each step t of the agent in order to obtain a reduction in the computational time.
- A negative reward, r_{obst}, is given if a collision is detected between the agent ($\mathbf{q}_{agent_t}$) and the obstacles ($obst$).
- A positive reward, r_{target}, is given upon reaching the target ($\mathbf{q}_{target_t}$).
- A negative reward is given, $r_{TPE} = -\left\|\mathbf{p}(\mathbf{q}_t) - \mathbf{p}(\mathbf{q}_{agent})\right\|$, upon reaching the target in order to minimize the difference between the target ($\mathbf{p}(\mathbf{q}_t)$) and the agent final position ($\mathbf{p}(\mathbf{q}_{agent})$).

The optimal parameters of the $R(\tau) = r_t$, obtained with an empirical method, are reported in Table I.

TABLE I

REWARD FUNCTION PARAMETERS VALUES

$r_{stepmax}$	r_{obst}	r_{target}	t_{max}
-1	-1	+3	5000

In the training process the agent learns to maximize its cumulative reward based on a PPO, taking into account the environment state. During the training phase the BC, which corresponds to the intrinsic reward, is active for all the steps (t). Values associated to the training parameters can be found in Table II

TABLE II

DEPLOYED LEARNING CONFIGURATION.

Parameter	***strength***	***gamma***
BC	0.5	
extrinsic	1.0	0.99
intrinsic	0.02	0.99
GAIL	1.0	0.99

C. Actuation plant and control

A sheath catheter and a delivery catheter are included in the MC system. During the operation, the delivery catheter is inserted into the sheath catheter and deploys the clip to the desired position above the mitral valve. After that, the surgeon can regulate the clip clamping the mitral valve using the so-called delivery catheter handle.

In this paper, we propose a catheter actuation plant ((Fig.4 A) with three degrees of freedom: medio-lateral bending in the coronal plane, anterior-posterior bending in the sagittal plane, and translational insertion inside the sheath catheter. As a result, we design a motorized stabilizer, which is composed of three primary mechanical and electrical elements:

- Nema 23 Stepper motors (JoyNano) to pull the tendons and to allow for medio-lateral and anterior-posterior bending. The control precision ($1.8^\circ \pm 0.09^\circ$ for each step) and maximum holding torque (0.6 Nm) are the most important criteria to consider when selecting stepper motors . Each motor is controlled by a DM556 driver (Jadeshay), which has eight current levels with a resolution of 0.5 A. An Arduino UNO board (Arduino) is used to output the control signal (Fig.4 B);
- Nema 17 linear actuator (SainSmart) that converts the rotation of the motor's shaft into a translation movement

in order to precisely insert the delivery catheter inside the sheath catheter. There are two critical requirements: great precision (±0,03 mm on the required position) and the ability to carry a structure, which is the maximum axial load of 10 kg;

- Oldham adapters-couplings (RS components) that connect the shaft of the delivery catheter to the shafts of the motor. This type of adapters is chosen because of its capacity to resist a 5mm misalignment between shafts.

We designed the entire system in Solidworks (Dassault systems) and 3D printed all of the structural components of the motorized stabilizer (Ultimaker 3S, Ultimaker B.V.) using PLA materials (Fig. 4 C, D). Then, we assembled the catheter actution plant and inserted it inside the sheath catheter, which was placed on a phantom (Fig. 4 E). In addition, we tracked the position of the sheath with the Aurora EM tracking system (NDI, Inc.). The Aurora generator was placed aside the tip of the catheter to generate the magnetic field. The EM sensor was attached to measure the real pose of the tip of the catheter with respect to its base, i.e., the insertion point in the septum (Fig.4 F). All the algorithms were run on a PC running Ubuntu 20.04 (PC1), except for the path planner, which run in Unity on a different PC (PC2) equipped with a Windows 10 operating system. Those two computers were connected by an Ethernet cable and exchanged data by ROSbridge based on the Web-Socket communication protocol (Fig.4 G).

Furthermore, a PID controller was employed to calculate the mismatch between the desired position ($\mathbf{p_d}$) and the measured position ($\mathbf{p_m}$) and to apply a correction to increase the control precision. We used the Ziegler–Nichols method to tune the parameters of the PID controller, i.e., the coefficient of the proportional term (K_p), of the integral term (K_i), and of the derivative term (K_d).

Finally, the control scheme was implemented thanks to the integration of the inverse kinematic model and the actuation leds, which was accomplished using the ROS (Robot Operating Syste, Noetic) middelware framework represented in Fig. 5. Starting from the desired pose ($\mathbf{p_d}$), the inverse kinematic model computes the tendons' displacement ($\Delta\mathbf{d_i}$) that is provided to the plant. When the actuation is complete, the ROS topic "Finish actuation" is activated, and the PID controller starts to compare the desired pose ($\mathbf{p_d}$) to the measured one ($\mathbf{p_m}$), generating a new position ($\mathbf{p_r}$) that is conveyed to the inverse kinematic model, allowing the adjustment of the position. When the error of the clip pose falls below a predefined threshold, the "conclusion" ROS topic confirms the end of the robotic procedure.

IV. Experimental Setup and Protocol

A. Experimental Setup

To evaluate the robotic-assisted surgical system, an experimental platform including a silicon anatomical phantom was developed (Fig.6). The platform consisted in a deformable model of femoral vena cava and inferior vena cava and in rigid replicas of the fossa, i.e., the portion of the interatrial

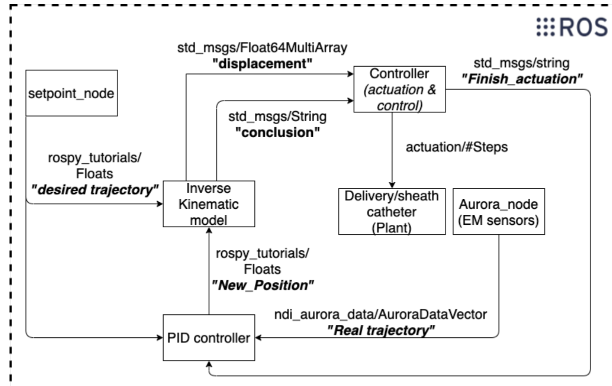

Fig. 5. ROS network scheme

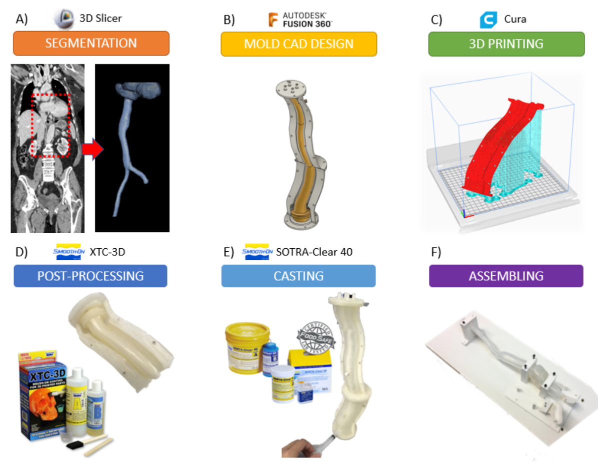

Fig. 6. Workflow process for the patient-specific physical phantom. (A) Segmentation and building up the 3D anatomical model; (B) Casting mold and components CAD design; (C) 3D printing components; (D) Post-processing for the casting mold; (E) Perparing silicon and casting; (F) Assembling all the components

septum that is punctured by the catheter in the real procedure, and of the mitral valve. Three holes were present in the fossa replica, as if the latter was already punctured. The geometry of the vessel and the mutual position of vessels, fossa and mitral valve was defined based on CT images to replicate this key feature of the real intracardiac structure. To this aim, manual segmentation of CT images and smoothing of the reconstructed geometry were performed in 3D Slicer (Fig.6 A). The 3D computational model was imported into Fusion 360 (Autodesk) to define the geometry i) of the internal and external casts devoted to the molding of the deformable vessel and ii) of the rigid components of the set-up, i.e., mitral valve, fossa, housings designed to hold the deformable vessel, and heart base (Fig.6 B). Of note, the heart base included four pillars devoted to performing the subsequent calibration procedure.

Casts and rigid components were 3D printed (Ultimaker 3S, Ultimaker B.V.) by PLA and the Breakaway materials as support because of their geometrical complexity (Fig.6 C). The internal cast model and the inner surface of the external cast were cured by polishing with sandpaper and covered with epoxy resin XTC-3D (Smooth-On, Inc.) to decrease the surface roughness of the cast model and hence increase the transparency of the final silicon model (Fig.6 D). SORTA-clear 40 silicone (Smooth-On, Inc.) was injected into the constructed cast mold, and polymerized at room temperature over 16 hours to yield the patient-specific silicone model (Fig.6 E). The complete phantom was finally assembled (Fig.6 F).

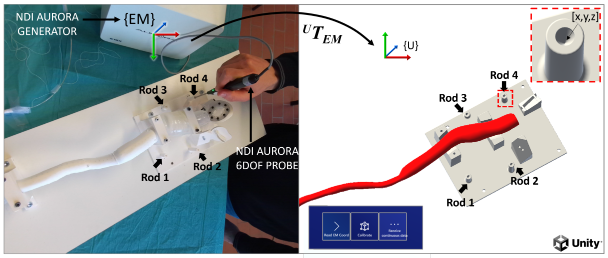

Fig. 7. Complete phantom (left) and corresponding virtual model (right). To couple the position of the four pillars in the $\{\mathbf{U}\}$ coordinate system with the position of the sensor in the $\{\mathbf{EM}\}$ coordinate system, the probe sensor was positioned in the cavities on the tip of the pillars according to a predetermined sequence, so that the respective positions could be related to those in the virtual model with an *ad hoc* user interface in the unity scene.

Moreover, a calibration procedure was executed to compute the registration matrix that aligns the position of the EM sensor navigating in the physical phantom with respect to the Unity scene in which both a virtual sensor and phantom are represented. The transformed position from the EM sensor was then received at each frame in a continuous manner in the Unity scene. Every virtual object rendered in the Unity scene was positioned with respect to a global left-hand coordinate system $\{\mathbf{U}\}$. The 5DoF sensor position, on the other hand, was represented with respect to Aurora right-hand global coordinate system $\{\mathbf{EM}\}$, based on the characterized measurement volume of the field generator. To register these two spaces and then achieve a calibration procedure, the location of fiducial points whose coordinates are known in both spaces is required. For this reason, the heart base in physical phantom was equipped with four pillars known position and height and a conical cavity at the top (Fig. 7 Left). The conical cavity was intended to accommodate the tip of the EM sensor probe with which the calibration procedure was executed, stabilizing its position while handled by the user. The digital model of the base (Fig. 7 Right) containing the four rods was included in the unity scene so as to have a unique association between the position of the physical rods touched by the EM sensor and the same represented in the virtual scene.

For each of the four positions, the user interacting with a virtual interface acquired the position of the sensor from the ROS node while the tool was stationary in one of the physical rods. Ten sensor positions were read each time and averaged to cancel out possible noise from the sensor. The probe was then moved in all the remaining rods to have four completely different coordinates in the space from the sensor $\mathbf{p_i}(i=1,\dots 4)$, and from the unity scene $\mathbf{q_i}(i=1,\dots 4)$. Upon acquiring the four different positions, the two sets of corresponding 3D points were processed to find the optimal rotation ($\mathbf{R}$) and translation ($\mathbf{T}$) matrix that aligned the positions received from the sensor in the $\{\mathbf{EM}\}$ space to the $\{\mathbf{U}\}$ space. An algorithm to find the least-squares solution of R and T, which is based on the singular value decomposition (SVD), was applied to compute the registration matrix $^{U}T_{EM}$.

$$\mathbf{q}_i = {}^{U}\mathbf{T}_{EM} \bullet \mathbf{p}_i \tag{7}$$

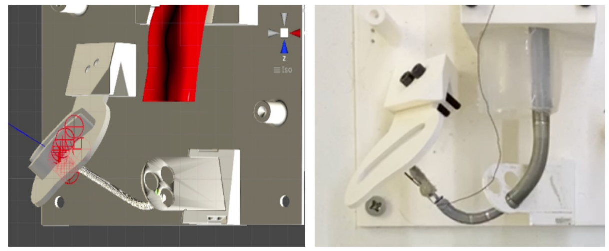

Fig. 8. Validation experiment: given a target on the mitral valve, the path planner can generate an optimized path in the Unity environment and forward the data to the actuation plant, which drives the delivery catheter to autonomously deposit the clip in the target position.

Once the calibration procedure is completed, a virtual Game Object in the Unity scene dynamically matches its moving physical counterpart (the sensor's tip). Then the experiment can be carried out under the constrain of the sheath catheter inside the phantom. In the Unity environment, a target position is set for the artificial intelligent agent to create a optimized path, which is a series of desired position ($\mathbf{p_{d_i}}$) for the actuation plant. Moreover, one 5-DOF EM snesor with the accuracy of 0.7 ± 1.4mm, is mounted to the tip of the delivery catheter to measured the position in real-time and feedback to the controller (Fig. 8). Finally, the tip positions of the catheter are recorded by a 6-DOF EM probe, which has a higher position accuracy of 0.48 ± 0.88mm.

B. Performance Metrics

1) Path Planner Performance Metrics: For the pre-operative Path Planner validation two different settings were compared for the path search:

- Method 1: Manual (state of the art for the surgery).
- Method 2: BC + GAIL

Those two settings were tested m times (with $1 \leq m \leq 10$) in the intracardiac phase starting from a starting configuration ($\mathbf{q_s}$) (placed on the septum) to a the target ($\mathbf{q_s}$) (place on the mitral valve). Obtaining in output m pre-operative manual path ($\mathbf{P_m^{manual}}$) applying the first manual method and m pre-operative automatic path ($\mathbf{P_m^{BC+GAIL}}$) applying the second automatic method.

The results obtained from each manual ($\mathbf{P_m^{manual}}$) or automatic ($\mathbf{P_m^{BC+GAIL}}$) experiment were analysed according to the following metrics:

1) The minimum distance, (d_{min}), and average distance (d_{avg}), from obstacles ($obst$), in [mm]
2) The maximum curvature, ($curv$) in [mm^{-1}] they should be smaller than the catheter's maximum curvature, which is to 0.02618 mm^{-1}.

3) The total length, ($length$), of the path, in [mm]: it shouldn't exceed the actual length of the catheter, which is 70 mm.
4) The success rate, (*SR*): to ensure that the method is reliable the success rate must be as high as possible.
5) The target positioning error, (tpe), in [mm], i.e., the accuracy of the catheter's final position with respect to the target's position.
6) The target orientation error, (toe), in [mm], i.e., the difference between the orientation of the target and the orientation of the catheter pointing at the target in its final pose. These last two values should be the smallest possible.

2) Position Performance Matrix: To evaluate the fidelity and the performance of the system, we fed the actuation plant with a set of the desired position ($\mathbf{p_{d_i}}$) on the trajectory obtained from the path planner. The position accuracy in all directions was quantified by the position mismatch ($\mathbf{e_i}$) between the tip position measured in the Cartesian space ($\mathbf{p_{m_i}}$) and the desired one ($\mathbf{p_{d_i}}$). We also studied the improvement of the controller on the positioning by comparing the outcomes of the open-loop and PID feedback control algorithms.

V. RESULTS

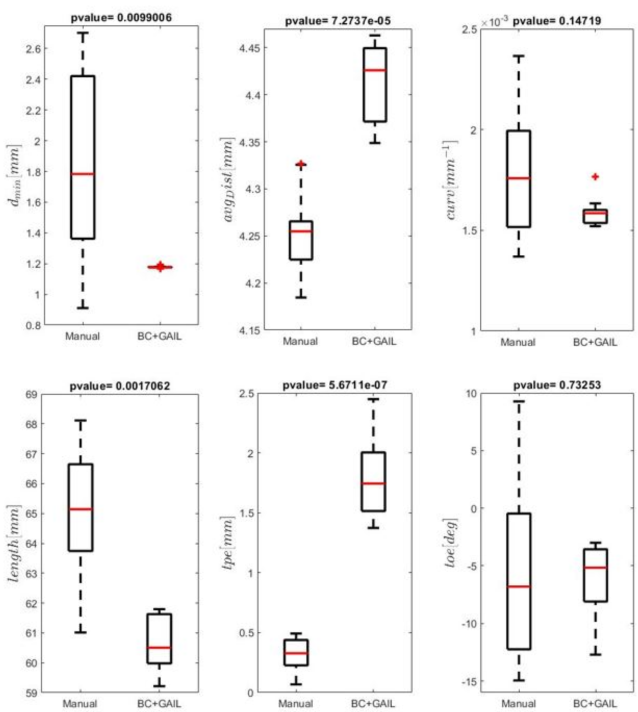

Fig. 9. Manual and Path Planning results comparison in terms of minimum distance (d_{min}), average distance (*avgDist*), curvature (*curv*), length (*length*), target position error (tpe) and target orientation error (toe).

Fig. 9 shows the comparison between the Manual and the BC+GAIL Path Planner. The Manual approach shows higher values in terms of d_{min}, $curv$, $length$ and toe. A significant difference in d_{min} is found, where the Manual approach showed a mean value of 1.82±0.63 mm with respect to 1.18±0.01 mm for the BC+GAIL approach. Regarding the d_{avg} of the Manual approach has a mean value of 4.25±0.05mm and 4.41±0.04 mm for the BC+GAIL one. The BC+GAIL approach also shows lower values in terms of $curv$, where the maximum curvature is 0.0016±7.17e-05 mm^{-1} while the Manual one gives a value of 0.0018±3.19e-04 mm^{-1}. BC+GAIL approach leads to shorter path lengths ($length$=60.63±0.96 mm) as compared to the manual approach ($length$=64.99±6.11 mm). The Manual tpe is 0.32±0.14mm, which is lower than the result obtained by the BC+GAIL the path planner of 1.79±0.35 mm. However, the toe shows very similar values, in which the manual approach reaches the target with an angle error of $-5.17\pm7.74°$, and the BC+GAIL one presents an error of $-5.99\pm3.10°$. We also analyze the time required to compute the path, from the starting configuration ($\mathbf{q_s}$) to the target one ($\mathbf{q_t}$), and we got 8.9080±0.2258s for the manual approach, and almost the same for the BC+GAIL one, resulting in 8.9140±0.0786 sec with the speed set equal to 10 mm/s.

The results in Fig 10 indicate that the proposed approach is able to position the tip of the catheter within an acceptable range. The average position error with the feedback controller in X, Y, Z directions are 1.12 ± 0.75mm, 1.09 ± 0.68mm, 1.66 ± 0.62mm respectively. The maximum position error happens in the Z direction, which is 2.64mm. Compared to the results of the open-loop control, the PID controller can reduce the average position error of 32.68% in all directions.

VI. CONCLUSION AND DISSCUSION

This paper presents the preliminary validation results of a robotic-assisted system comprised of an analytical inverse kinematic model based on the CRT; a pre-operative path planner based on the inverse reinforcement learning, and a catheter actuation plant with a PID feedback controller. Experimental results suggested the feasibility and effectiveness of the implemented system for SIC treatment.

However, the noise in the EM sensor introduced significant uncertainty in the measurement of catheter tip position. The maximum distance error and the largest average error were both in the Z direction, suggesting that friction between the sheath catheter and the delivery catheter should be compensated for.

Further work will focus on how to improve the system structure and assembly procedures to increase the accuracy of the delivery system. Additionally, the hysteresis effect will be investigated in the kinematic model to deal with nonlinearity. Moreover, the measured position could be fed to the path-planner to update the optimized path in real-time. Furthermore, augmented reality devices will be employed to provide more intuitive navigation experience for the operator.

REFERENCES

[1] P. Lanzer, "Textbook of catheter-based cardiovascular interventions," *Cham: Springer International Publishing*, 2018.

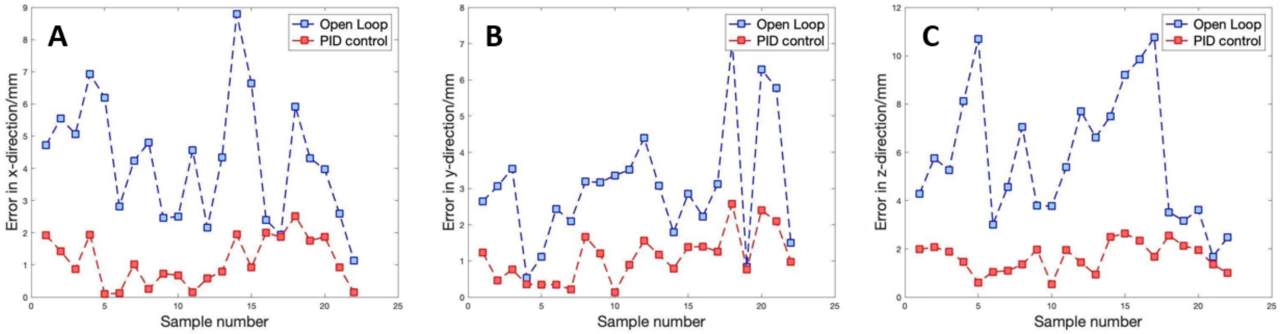

Fig. 10. Comparison of position error between the open-loop control and the feedback control algorithm: (A) shows the position error in the X-direction; (B) shows the position error in the Y-direction; (C) shows the position error in Z-direction.

[2] A. K. Chhatriwalla, S. Vemulapalli, D. R. J. Holmes, D. Dai, Z. Li, G. Ailawadi, D. Glower, S. Kar, M. J. Mack, J. Rymer, A. S. Kosinski, and P. Sorajja, "Institutional experience with transcatheter mitral valve repair and clinical outcomes: Insights from the tvt registry," *JACC Cardiovascular Interventions*, vol. 12(14), pp. 1342–1352, 2019.

[3] H. Eggebrecht, S. Schelle, M. Puls, B. Plicht, R. S. von Bardeleben, C. Butter, A. E. May, E. Lubos, P. Boekstegers, T. Ouarrak, *et al.*, "Risk and outcomes of complications during and after mitraclip implantation: experience in 828 patients from the german transcatheter mitral valve interventions (trami) registry," *Catheterization and Cardiovascular Interventions*, vol. 86, no. 4, pp. 728–735, 2015.

[4] P. Rao, Q. Peyron, S. Lilge, and J. Burgner-Kahrs, "How to model tendon-driven continuum robots and benchmark modelling performance," *Frontiers in Robotics and AI*, vol. 7, p. 223, 2021.

[5] R. J. Webster III and B. A. Jones, "Design and kinematic modeling of constant curvature continuum robots: A review," *The International Journal of Robotics Research*, vol. 29, no. 13, pp. 1661–1683, 2010.

[6] H.-J. Su, "A pseudorigid-body 3r model for determining large deflection of cantilever beams subject to tip loads," 2009.

[7] R. J. Webster, J. M. Romano, and N. J. Cowan, "Mechanics of precurved-tube continuum robots," *IEEE Transactions on Robotics*, vol. 25, no. 1, pp. 67–78, 2008.

[8] D. C. Rucker and R. J. Webster III, "Statics and dynamics of continuum robots with general tendon routing and external loading," *IEEE Transactions on Robotics*, vol. 27, no. 6, pp. 1033–1044, 2011.

[9] Y. Ganji, F. Janabi-Sharifi, and A. N. Cheema, "Robot-assisted catheter manipulation for intracardiac navigation," *International journal of computer assisted radiology and surgery*, vol. 4, no. 4, pp. 307–315, 2009.

[10] G. Fagogenis, M. Mencattelli, Z. Machaidze, B. Rosa, K. Price, F. Wu, V. Weixler, M. Saeed, J. E. Mayer, and P. E. Dupont, "Autonomous robotic intracardiac catheter navigation using haptic vision," *Science robotics*, vol. 4, no. 29, p. eaaw1977, 2019.

[11] W. Chi, G. Dagnino, T. M. Kwok, A. Nguyen, D. Kundrat, M. E. Abdelaziz, C. Riga, C. Bicknell, and G.-Z. Yang, "Collaborative robot-assisted endovascular catheterization with generative adversarial imitation learning," in *2020 IEEE International Conference on Robotics and Automation (ICRA)*. IEEE, 2020, pp. 2414–2420.

[12] A. Segato, M. Di Marzo, S. Zucchelli, S. Galvan, R. Secoli, and E. De Momi, "Inverse reinforcement learning intra-operative path planning for steerable needle." *IEEE Transactions on Bio-medical Engineering*, 2021.

[13] J. Schulman, J. Ho, C. Lee, and P. Abbeel, "Learning from demonstrations through the use of non-rigid registration," in *Robotics Research*. Springer, 2016, pp. 339–354.

[14] W. Chi, J. Liu, H. Rafii-Tari, C. Riga, C. Bicknell, and G.-Z. Yang, "Learning-based endovascular navigation through the use of non-rigid registration for collaborative robotic catheterization," *International journal of computer assisted radiology and surgery*, vol. 13, no. 6, pp. 855–864, 2018.

[15] P. M. Loschak, L. J. Brattain, and R. D. Howe, "Algorithms for automatically pointing ultrasound imaging catheters," *IEEE Transactions on Robotics*, vol. 33, no. 1, pp. 81–91, 2016.

[16] J. Back, L. Lindenroth, K. Rhode, and H. Liu, "Model-free position control for cardiac ablation catheter steering using electromagnetic position tracking and tension feedback," *Frontiers in Robotics and AI*, vol. 4, p. 17, 2017.

[17] B. Yu, J. d. G. Fernández, and T. Tan, "Probabilistic kinematic model of a robotic catheter for 3d position control," *Soft robotics*, vol. 6, no. 2, pp. 184–194, 2019.

[18] S. N. Ha, "A nonlinear shooting method for two-point boundary value problems," *Computers & Mathematics with Applications*, vol. 42, no. 10-11, pp. 1411–1420, 2001.

[19] A. Gasparetto, P. Boscariol, A. Lanzutti, and R. Vidoni, "Path planning and trajectory planning algorithms: A general overview," *Motion and operation planning of robotic systems*, pp. 3–27, 2015.

[20] S. Pieper, M. Halle, and R. Kikinis, "3D slicer," in *2004 2nd IEEE international symposium on biomedical imaging: nano to macro (ISBI) (IEEE Cat No. 04EX821)*. IEEE, 2004, pp. 632–635.

[21] R. Schmidt and K. Singh, "Meshmixer: an interface for rapid mesh composition," in *ACM SIGGRAPH 2010 Talks*, 2010, pp. 1–1.

[22] W. Goldstone, *Unity game development essentials*. Packt Publishing Ltd, 2009.

[23] T. K. Devi, A. Srivatsava, K. K. Mudgal, R. R. Jayanti, and T. Karthick, "Behaviour cloning for autonomous driving." *Webology*, vol. 17, no. 2, pp. 694–705, 2020.

[24] J. Ho and S. Ermon, "Generative adversarial imitation learning," *Advances in neural information processing systems*, vol. 29, 2016.